INORGANIC CHEMISTRY FRONTIERS

RESEARCH ARTICLE

View Article Online
View Journal

Cite this: DOI: 10.1039/d5qi02127h

Water oxidation by Ni(II) amido-quinoline complexes

Monika,[a] Vasanthapandiyan Mari,[a] Pankaj Kumar,[b] Naiwrit Karmodak[a] and Basab Bijayi Dhar*[a]

Received 17th October 2025,
Accepted 28th November 2025

DOI: 10.1039/d5qi02127h

rsc.li/frontiers-inorganic

Ni(II) amido-quinoline complexes (**NiL1**, **NiL2**, **NiL3**) efficiently catalyze electrochemical water oxidation to O_2 in a non-aqueous medium, with water as the limiting reagent. Field emission scanning electron microscopy (FE-SEM) and energy-dispersive X-ray spectroscopy (EDX) revealed no deposition of a NiO_x film on the electrode, confirming the role of Ni(II) amido-quinoline complexes as true molecular electrocatalysts. Spectroelectrochemical studies revealed Ni(III) formation at the reaction onset. The redox-active amido-quinoline ligand participates in the oxidation, preventing the Ni(III) center from accessing higher oxidation states. From scan rate-dependent studies, rate constants (k_0) were found to be 1.42 M^{-1} s^{-1}, 1.05 M^{-1} s^{-1}, and 1.99 M^{-1} s^{-1} for **NiL1**, **NiL2**, and **NiL3**, respectively. DFT calculations revealed that the coupling of Ni–O$^{\bullet}$ and the adsorbed OH intermediate prefers the formation of a peroxy (NiL-OOH) intermediate over the electrochemical oxidation of Ni–O$^{\bullet}$ with a water molecule involving a proton-coupled electron transfer step. The charge density analysis suggested that the phenyl group in the **NiL3** complex reduces the electron density at the active metal centre and enhances the reactivity compared to the other complexes. Spin density analysis showed increased electron density at the O center of NiL(O$^{\bullet}$)OH, reducing the energy barrier for NiL-OOH formation on the **NiL3** complex.

Introduction

Over the past few decades, chemists worldwide have been working to develop sustainable energy conversion processes by performing water splitting in the presence of sunlight, using various transition metal catalysts. Water splitting into H_2 and O_2 is a multi-proton-coupled electron transfer (PCET) reaction and an energetically uphill process.[1,2] The critical step in this process is water oxidation (WO), which leads to O–O bond formation. In photosystem II, WO occurs *via* an oxygen-evolving complex (OEC) without producing long-lived intermediates like H_2O_2, with a turnover frequency (TOF) of 100–400 s^{-1}.[3,4] The OEC consists of metal-oxo clusters made from Earth-abundant manganese and calcium.[5]

Significant advancements have been made in the field of WO catalysis, particularly with the discovery of various homogeneous and heterogeneous catalysts containing transition metals and achieving relatively high turnover numbers (TONs ~10 000).[6,7] Many of these catalysts involve metal complexes of noble metals such as ruthenium (Ru)[8,9] and iridium (Ir),[10,11] as well as polyoxometalates (POMs) and transition metal oxide nanoparticles (NPs).[12] Homogeneous WO catalysts have certain advantages over heterogeneous ones in mechanistic studies. Research groups have explored the use of homogeneous WO catalysts based on transition metals like Mn,[13,14] Fe,[15,16] Co,[17,18] Ni,[19,20] and Cu,[21,22] with varying degrees of success (Scheme 1).

Water oxidation requires a thermodynamic potential of 1.23 V *vs.* NHE at pH 0, along with additional overpotential to overcome kinetic barriers. This high potential can sometimes cause total or partial ligand oxidation, leading to deactivation of the molecular catalyst. Such oxidation may promote the formation of metal oxides, which could be responsible for the observed WO catalysis.[23] Therefore, a deeper understanding of these processes is essential to identify the real catalytic species operating in each system and to provide valuable insights for designing more stable and active molecular catalysts. So far, Ru and Ir complexes have shown superior performance in WO catalysis, but their high cost limits commercial applications. As a result, molecular complexes based on Earth-abundant metals have been extensively studied due to their advantages, including lower cost, environmental compatibility, and controllable redox properties.

Recently, nickel (Ni), among the late first-row transition metals, has gained significant attention from the scientific community due to its diverse redox properties and the strong

[a]*Department of Chemistry, School of Natural Sciences, Shiv Nadar Institution of Eminence Deemed to be University, Delhi NCR, Gautam Buddha Nagar, Dadri, UP-201314, India. E-mail: basab.dhar@snu.edu.in, basabbijayi@gmail.com*
[b]*Department of Chemistry, Ashoka University, Delhi NCR, Sonipat, Haryana-131029, India*

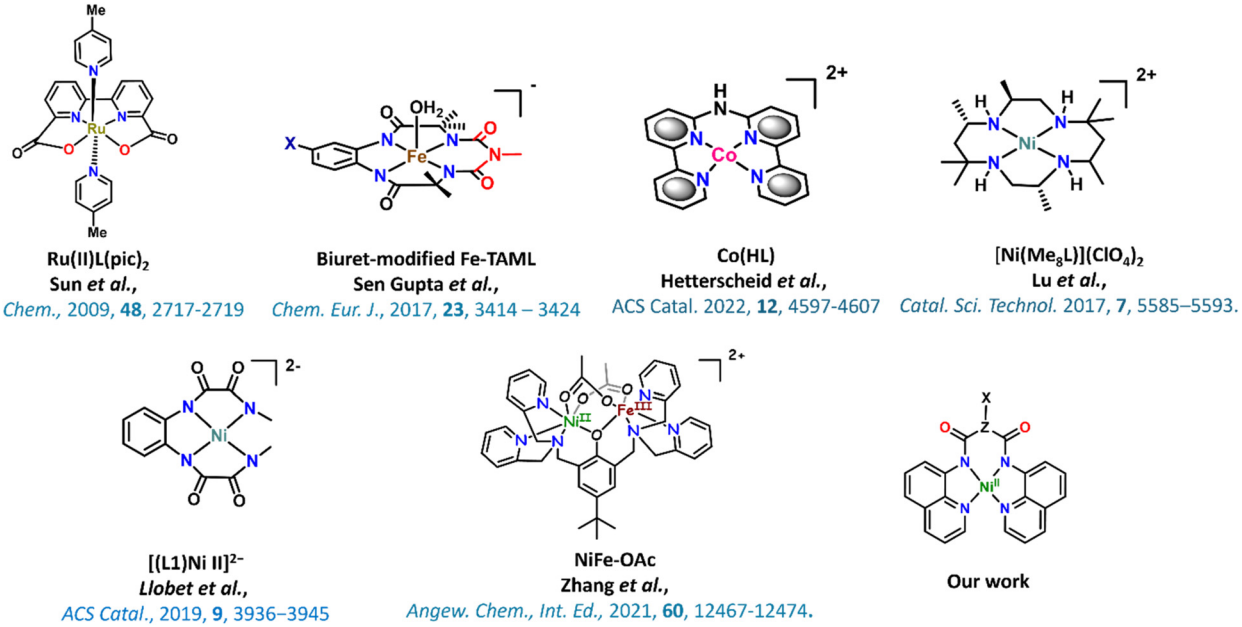

Scheme 1 Molecular complexes utilized for water oxidation in the last two decades.

oxidizing potential of its high-valence states. NiO_x and Ni $(OH)_2$ are commonly studied in heterogeneous catalysis. However, true homogeneous catalysis based on Ni complexes remains rare, making it a relatively unexplored field.[24] Over the years, various Ni(II) complexes have been reported for electrocatalytic water oxidation, including porphyrin-based systems, phenolate ligands and tetra-/di-amido frameworks (Table S1). Early reports, such as those regarding the [Ni(*meso*-L)](ClO_4) (*meso*-L = *meso*-5,5,7,12,12,14-hexamethyl-1,4,8,11-tetraazacyclotetradecane) complex, lacked direct evidence for high valent Ni(IV) intermediates and relied solely on DFT calculations.[24a] Similarly, porphyrin complexes demonstrated moderate activity (TOF ~0.67 s^{-1}) but did not provide experimental proof of reactive species or detailed mechanistic insights.[24b] Ni (II)-phenolate complexes exhibited limited catalytic activity (TOF ~0.15) and lacked direct experimental evidence for the formation of a high valent nickel intermediate or redox involvement of the non-innocent ligand.[24c] The work by Llobet *et al.* using a tetra-amido Ni(II) complex reported a high TOF and TON at high pH, particularly under heterogeneous conditions, yet mechanistic ambiguity persisted due to the mixed nature of the catalytic species.[24d] Ni complexes, such as [(**L1**)NiII]$^{2-}$ (**L1** = *o*-phenylenebis(oxamidate)) and its modified analogs [(**L2**)NiII]$^{2-}$ (**L2** = 4,5-dimethyl-1,2-phenylenebis(oxamidate)) and [(**L3**)NiII]$^{2-}$ (**L3** = 4-methoxy-1,2-phenylenebis (oxamidate)), have been evaluated as molecular water oxidation (WO) catalysts at basic pH.[25] Electrochemical studies and surface characterization techniques reveal the coexistence of two catalytic pathways: a homogeneous pathway driven by the molecular Ni complex and a heterogeneous pathway based on NiO_x. Experimental investigations suggest that the formation of a phenyl radical cation, along with the coordination of a hydroxo group to form $[(L)^{\bullet}Ni^{III}(OH)]^{-}$, is responsible for the electrocatalytic oxidation of water to O_2. In contrast, a water-soluble Ni(II) complex bearing a redox non-innocent tetra-amido macrocyclic ligand (TAML) has been found to be an efficient electrocatalyst for water oxidation in neutral potassium phosphate buffer.[26] This complex sustains a steady current of approximately 0.2 mA cm^{-2} for over 7 hours at 1.75 V *vs.* the NHE, without the formation of NiO_x. In the case of the heterobimetallic NiFe molecular platform (L = bpbp; 2,6-bis[[bis(2-pyridinylmethyl)amino]methyl]-4-(1,1-dimethylethyl)phenolate), mechanistic studies confirmed the sequential removal of electrons and protons from the phenolate and bridged OH units, forming a $[Ni^{II}(bpbp^{\bullet})(\mu\text{-}O)Fe^{IV}{=}O]^{2+}$ intermediate.[27] This intermediate further converts into a $Ni^{III}(\mu\text{-}O)Fe^{IV}{=}O$ species, which serves as the key intermediate for WO. The O–O bond forms *via* intramolecular oxyl-oxo coupling between the bridged O radical and the terminal $Fe^{IV}{=}O$ moiety. These findings highlight the importance of redox non-innocent ligands in the rational design of molecular WO catalysts, offering insights for future advancements in this area.

In this report, we highlight that amido-quinoline complexes of Ni(II) were successfully able to perform water oxidation at room temperature (RT). Unlike earlier reports, our study provides compelling experimental evidence of Ni(III) intermediates through spectroelectrochemical measurements, HR-MS, and O^{18}-labeling experiments. Furthermore, the redox-active ligand framework and structural features offer unique insights into the catalytic pathway, substantiating the novelty and significance of our findings. The role of ligands in the catalytic mechanism was evaluated using density functional theory (DFT).

Results and discussion

Synthesis and characterization of the ligands and Ni(II) complexes

Ligands **H_2L1** and **H_2L2** were synthesized according to a method we recently reported (Fig. S1).[28] Additionally, a new tetradentate amido-quinoline ligand, **H_2L3**, was synthesized by reacting two equivalents of 8-aminoquinoline with phenylmalonyl dichloride in the presence of triethylamine as a base, under an inert atmosphere (Scheme 2 and Fig. S2–S4). The solvent was then evaporated, and the residue was dissolved in dichloromethane, layered with diethyl ether, and left for crystallization. The characterization of ligand **H_2L3**, including HR-MS, ^{1}H, and ^{13}C NMR spectra, is described in the SI. The crystal structure of the ligand **H_2L3** is described in Fig. 1a (Table S2). Elemental analysis of **H_2L3** is given in the SI.

To synthesize the **NiL1**, **NiL2**, and **NiL3** complexes, the ligands (**H_2L1–L3**) were reacted with one equivalent of Ni(II)Cl_2 salt in DMF at room temperature, using triethylamine as a base. The complexes were isolated as dark orange crystals suitable for single-crystal X-ray diffraction (SC-XRD) analysis. These complexes were characterized by single-crystal X-ray structure analysis (Fig. 1 and Table S2), UV-Vis (Fig. 2a and Fig. S5a), HR-MS (Fig. S5b), cyclic voltammetry (CV) (Fig. 2b) and NMR (Fig. S6). The single-crystal X-ray structures of two complexes **NiL1** and **NiL2** were previously reported by our group.[28a] The SC-XRD analysis reveals that, like **NiL1** and **NiL2**, **NiL3** exhibits a similar coordination environment (Fig. 1 and Table S2). The ligand binds to the nickel ion through two neutral quinoline nitrogen atoms and two deprotonated amide nitrogen atoms, forming a distorted square planar NiN_4 core with a tetrahedral distortion parameter (τ_4)[29] value of 0.171 and a four-coordinate geometric index (τ_δ) of 0.159 (Table S3). This coordination generates two five-membered chelate rings and one six-membered chelate ring around the metal center. The Ni–N_{amide} bond is shorter than the Ni–$N_{quinoline}$ bond due to the higher electron density on the amide nitrogen, which arises from resonance with the carbonyl group. Additionally, the electronic effects of the amide group, including possible resonance interactions with the metal center, influence the six-membered chelate ring. The angle of the $N_{quinoline}$–Ni–N_{amide} five-membered chelate ring is less than 90°, indicating more constrained chelation around the metal center. The ^{1}H NMR analysis indicated that the nickel center is diamagnetic. The absence of the amide (N–H) proton signal at 5.1 ppm confirmed the deprotonation of the amide group during complex formation (Fig. S6). Furthermore, the downfield shift of quinoline ring proton signals compared to the free ligand indicates coordination of the ligand to the nickel ion.

The UV-Vis spectra of the Ni(II) complexes were recorded in acetonitrile (Fig. 2a). All three complexes displayed similar spectral features, with two distinct absorption bands: an intense band in the UV region (230–320 nm), attributed to a ligand ($\pi \rightarrow \pi^*$) transition, and a broad lower-energy band in the visible region (420–430 nm), ascribed to a ligand-to-metal charge transfer (LMCT) transition from the quinoline to the metal d orbitals. In the presence of water, a blue shift was observed in UV-Vis spectra of the Ni(II) complexes (Fig. S5a). This indicates that modifications of the molecular structure

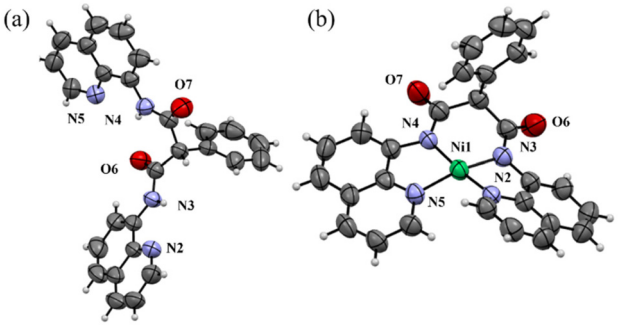

Fig. 1 ORTEP plots of (a) **H_2L3** (CCDC 2444267) and (b) **NiL3** (CCDC 2419464) shown at the 50% probability level with only heteroatoms labelled. Selective interatomic bond distances and angles for **NiL3**: Ni(1)–N(2) = 1.906 Å, Ni(1)–N(3) = 1.885 Å, Ni(1)–N(4) = 1.881 Å, Ni(1)–N(5) = 1.909 Å, [N(2)–Ni(1)–N(3)] = 83.8°, [N(2)–Ni(1)–N(4)] = 173.1°, [N(2)–Ni(1)–N(5)] = 97.9°, [N(3)–Ni(1)–N(4)] = 95.6°, [N(3)–Ni(1)–N(5)] = 162.9°, and [N(4)–Ni(1)–N(5)] = 84.7°.

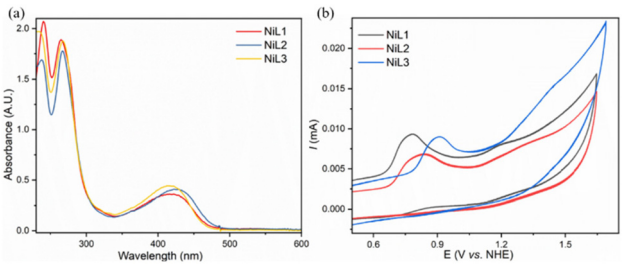

Fig. 2 (a) UV-Vis spectrum of 0.1 mM **NiL1** (red), **NiL2** (blue), and **NiL3** (yellow) in ACN. For **NiL3** {λ_{max}, nm (ε/M^{-1} cm^{-1})}: 238 nm (19 000 M^{-1} cm^{-1}), 279 nm (18 000 M^{-1} cm^{-1}), and 416 nm (5000 M^{-1} cm^{-1}). (b) Cyclic voltammograms of all three complexes in anhydrous ACN at the scan rate = 100 mV s^{-1} with 0.05 M ^{n}Bu_4NPF_6 as a supporting electrolyte. Glassy carbon (GC) was used as a working electrode, and Pt was used as the counter electrode.

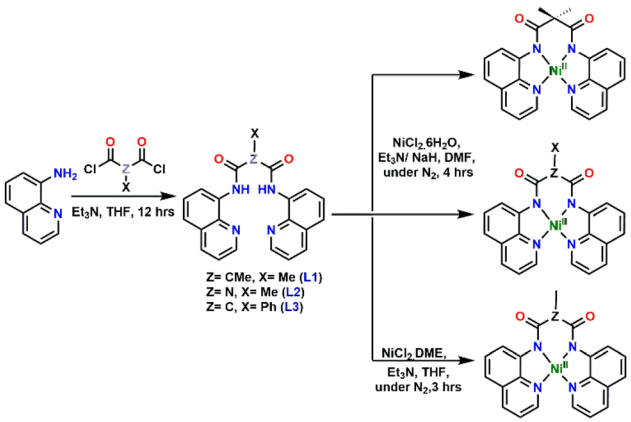

Scheme 2 Synthetic scheme of the ligands (**L1**, **L2** and **L3**) and the complexes (**NiL1**, **NiL2**, **NiL3**).

are due to the surrounding environment changes due to interaction with water. Elemental analysis of **NiL3** was carried out to check the purity of the sample. Details are given in the SI.

Electrocatalytic water oxidation by Ni(II) complexes

The redox properties of the complexes were investigated by CV in dry acetonitrile with 0.05 M tetra-butyl ammonium hexafluorophosphate ($^{n}Bu_4NPF_6$) employed as the supporting electrolyte and using Ag/Ag^{+} as a reference electrode at room temperature (Fig. 1b). Fig. 2b shows the CVs of Ni(II) complexes recorded in acetonitrile. Upon anodic scan for complex **NiL1** (Fig. 3), a well-defined oxidation wave is observed at 0.78 V *vs.* NHE, which can be assigned to Ni^{II}/Ni^{III} oxidation. In the absence of water, the second oxidation wave appears at 1.26 V. Upon the addition of 300 mM water, the second oxidation wave became a pronounced catalytic wave compared to the background at E = 1.32 V *vs.* NHE. This observation indicates that an electrocatalytic process occurs at this potential and we assigned this oxidation wave as a ligand-centered oxidation event.

The oxidation peaks are more distinctly observed in the Differential Pulse Voltammetry (DPV) results shown in Fig. S7a. DPV highlights the initial oxidation event and the rise in current in the second oxidation event upon adding water in **NiL1**. Incremental addition of water to an acetonitrile solution of complex **NiL1** revealed a rise in irreversible current with an onset potential of 1.03 V (Fig. 3 and Fig. S7b). This current increase is attributed to the water oxidation reaction. Additionally, the oxidation potentials of the ligand-based process were observed to be shifted cathodically with the incremental addition of water. Under the same experimental conditions, complexes **NiL2** and **NiL3** display two oxidation waves assigned to Ni^{II}/Ni^{III} and ligand-based oxidation at 0.82 and 0.87 V, and 1.31 and 1.28 V (Table 1), respectively (Fig. S8 and S9).

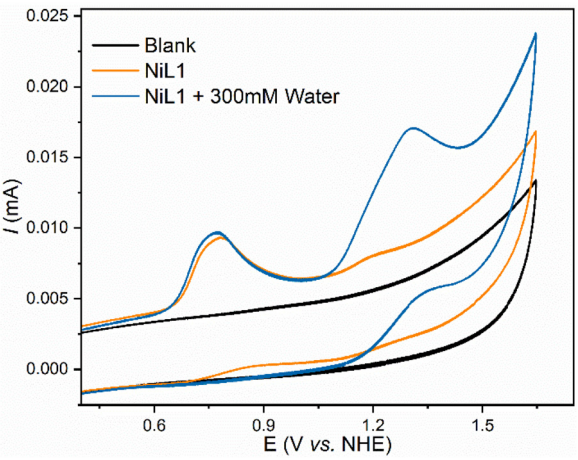

Fig. 3 Cyclic voltammograms of complex **NiL1** (0.2 mM) and electrocatalytic water oxidation upon addition of 300 mM water (scan rate of 100 mV s^{-1}).

Table 1 Overview of potential values for Ni(II) complexes after adding 300 mM water as measured by cyclic voltammetry

Complex	1st oxidation peak potential value (Ni^{II}/Ni^{III})	2nd oxidation peak potential value (ligand-based)
NiL1	0.78	1.32
NiL2	0.82	1.31
NiL3	0.87	1.28

Scan rate-normalized cyclic voltammograms ($i/\nu^{1/2}$) recorded at varying scan rates indicate that the first oxidation wave corresponds to an irreversible diffusion-controlled proton-coupled electron transfer process at the electrode for all the molecules. The peak current i_p exhibits a linear relationship with the square root of the scan rates, $\nu^{1/2}$ (Fig. 4 and Fig. S10, S11), according to the Randles–Ševčík equation, eqn (1),[30] where n is the number of electrons involved during the corresponding process ($1e^{-}$), ν is the scan rate (100 mV s^{-1}), F is the Faraday constant (96 500 sA mol^{-1}), A is the surface area of the working electrode (0.07 cm^2), [Ni] is the concentration of the nickel complexes used during the process (mol cm^{-3}), R is the ideal gas constant (8.314 J mol^{-1} K^{-1}), and T is the temperature (298 K). Normalized CVs of scan rate variation for all three complexes are given in Fig. S12.

$$i_p = 0.46nFA[\mathrm{Ni}]\left(\frac{D_{\mathrm{Ni}}nF\nu}{RT}\right)^{\frac{1}{2}} \quad (1)$$

The square of catalytic peak current ${i_{cat}}^2$ changes proportionally with water concentration [H_2O] (80–1200 mM) with saturation at higher water concentrations (Fig. 5a and b), which suggests the involvement of a single water molecule in a rate law. However, i_{cat} varies linearly with complex concentration [**NiL1**] (Fig. 5c and d). Similar behaviour was observed in the case of **NiL2** and **NiL3** (Fig. S13 and S14). These findings support an electrocatalytic mechanism for water oxidation, where the rate-limiting step involves the transfer of an oxygen atom to water from the high-valent metal oxo reactive intermediate, as described by the rate law in eqn (2).[31a]

$$\mathrm{Rate} = k_0[\mathrm{Ni}][\mathrm{H_2O}] = k_{\mathrm{cat}}[\mathrm{Ni}] \quad (2)$$

The dependence of catalytic current on complex concentration can be expressed by eqn (3)[31b] where n is the number

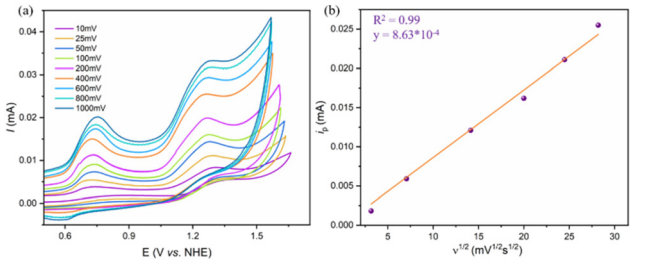

Fig. 4 (a) CV of scan rate variation of **NiL1** (0.2 mM) with 300 mM water added to it. (b) Peak catalytic current response with respect to $\nu^{1/2}$.

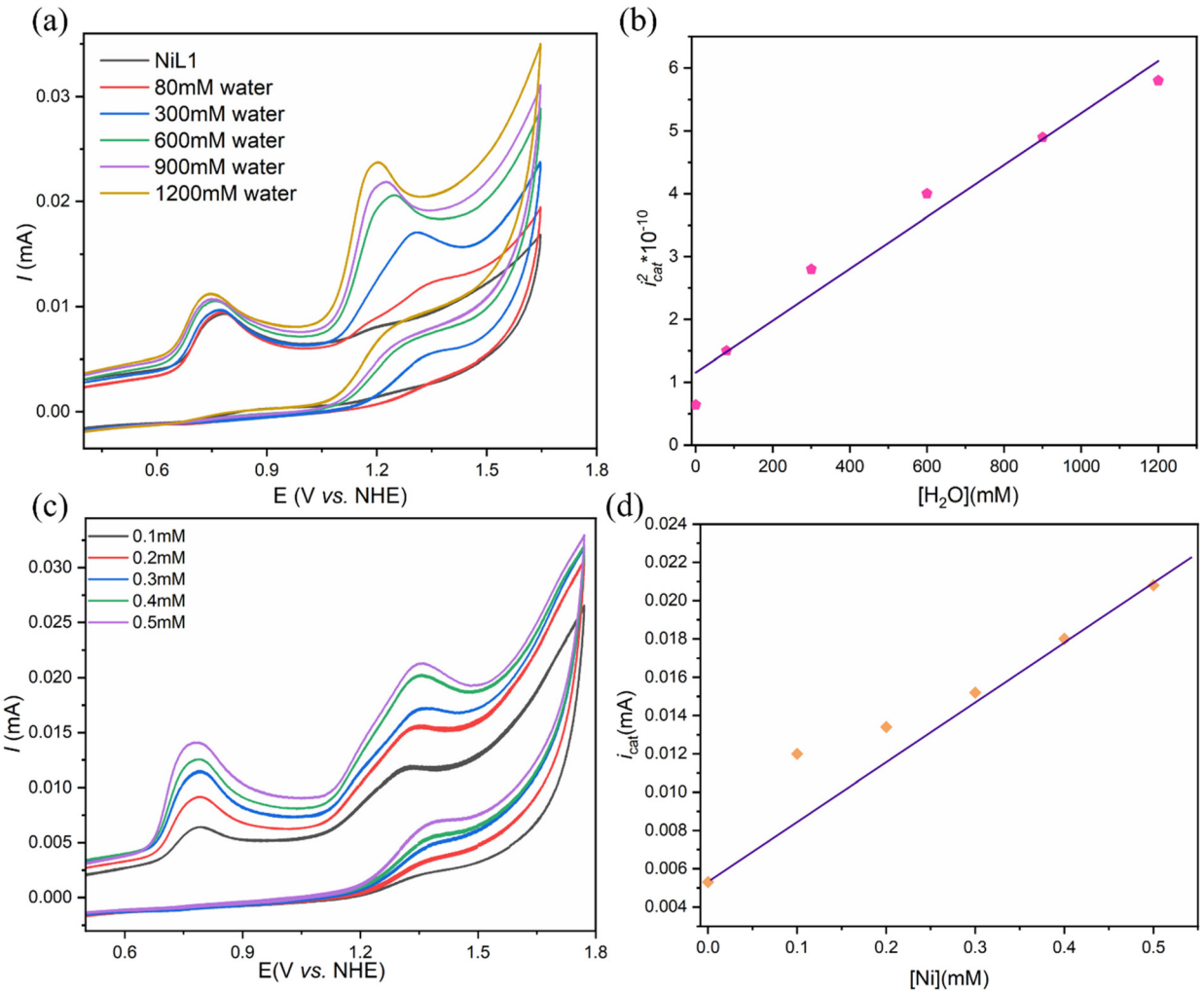

Fig. 5 (a) CV for **NiL1** (0.2 mM) upon adding different amounts of water. (b) Plot of $(i_{cat})^2$ (*vs.* NHE) *vs.* [H_2O]. (c) CVs for complex concentration variation of **NiL1**. (d) Plot of i_{cat} at 1.32 V (*vs.* NHE) *vs.* [**NiL1**].

of electrons involved during the catalytic process ($4e^-$) and k_{cat} is the rate constant for the water oxidation reaction:

$$i_{cat} = nFA[\mathrm{Ni}](k_{cat}D_{Ni})^{1/2} \quad (3)$$

Additionally, from the scan rate dependence study for **Ni(II) L1** in the absence of water, we observed no catalytic current generation (Fig. S7c).

Characterization using spectroelectrochemistry and spectrochemical titration

A spectroelectrochemical technique was employed to characterize the oxidized species generated from Ni(II) complexes during electrochemical water oxidation. The initial absorption spectrum of the **NiL1** complex shows a highly intense band at 268 nm and a broad band at 428 nm. During controlled potential electrolysis (CPE) at 0.78 V *vs.* NHE, time-dependent UV-Vis spectral change analysis was carried out in 1 minute intervals for 30 minutes. In Fig. 6a, we have given the spectra at 0 min, 5 min, 10 min, 15 min, 20 min, 25 min, and 30 min, respectively. A new broad band begins to grow at 318 nm, accompanied by multiple isosbestic points at 290 and 350 nm, indicating significant changes in the absorption spectrum. This transformation suggests the formation of a new species, possibly the active Ni(III) species involved in the water oxidation process (Fig. 6a). Moreover, charge *vs.* time and current *vs.* time plots for the CPE process are given in Fig. S15. Detailed calculation is provided in the SI.

To further confirm our assumption, 0.2 mM **NiL1** was spectrochemically titrated using ceric ammonium nitrate (CAN), a one-electron oxidizing agent. Upon incremental addition of CAN from 0.1 equivalent to 1 equivalent, gradual changes in the intensity of the π–π* band at 180 nm and the LMCT band at 400 nm were observed, along with the appearance of a prominent new band at 320 nm (ε = 8380 M^{-1} cm^{-1}) (Fig. 6b). The UV-Vis features of the Ni(III) species produced by spectrochemical titration align with those observed during CPE, indicating that the same oxidized species are formed both chemically

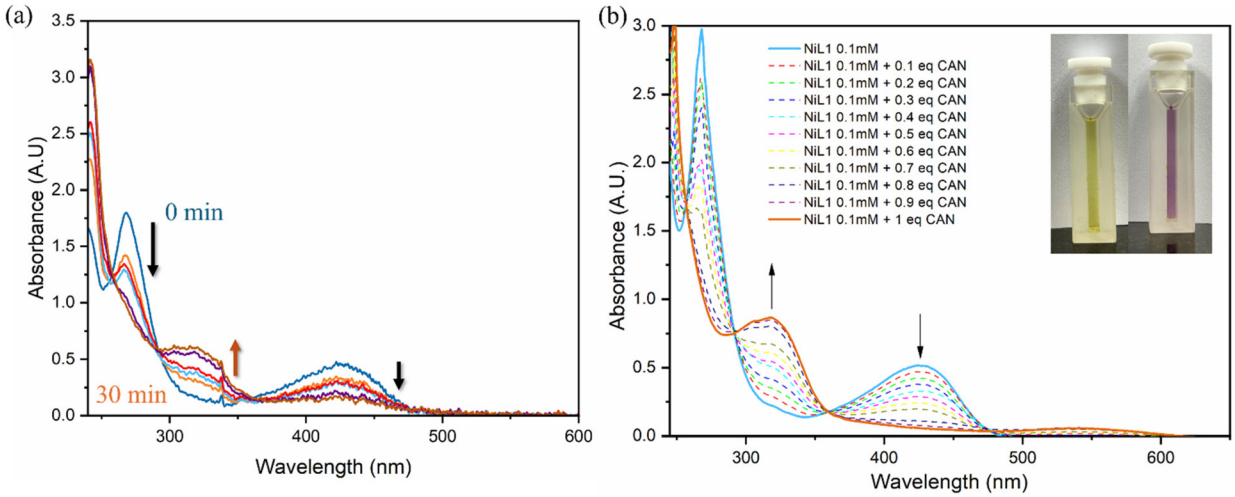

Fig. 6 (a) UV-vis spectral changes of **NiL1** (0.025 mM) with 0.05 M $^{n}Bu_4NPF_6$ as a supporting electrolyte during controlled potential oxidation at 0.77 V *vs.* NHE in ACN. (b) UV-Vis spectral changes of **NiL1** (0.1 mM) in ACN titrated with different concentrations of ceric ammonium nitrate (CAN). Inset: the colour change occurs from greenish yellow to violet when 1 equivalent of CAN was added to **NiL1**.

and electrochemically. An HR-MS study also confirmed the formation of [Ni(III)L1]NO_3 when titrated with 1 equivalent of CAN (Fig. 7a and Fig. S16). The plot of absorbance at 320 nm *vs.* equivalent of CAN is given in Fig. S17. To find out the kinetic stability of the high valent Ni(III) species, the spontaneous decay of [Ni(III)L1]NO_3 was studied using UV-Vis spectroscopy by monitoring the decrease at 320 nm (Fig. S18a and b) at RT up to 2400 s. The initial rates for various concentrations of **NiL1** (varied from 0.02 mM to 0.1 mM) were measured and then plotted with respect to [**NiL1**] for finding the first order rate constant. The first order rate constant for the decay was found to be 1.02×10^{-5} s^{-1} (Fig. S18c).

Additionally, electrochemical measurements using cyclic voltammetry (CV) of **NiL1** complexes were performed after titration with CAN. When 1 equivalent of CAN was added to a 0.2 mM **NiL1** solution with 0.05 M $^{n}Bu_4NPF_6$ as a supporting electrolyte, it exhibited one reversible redox wave at 0.86 V and an irreversible wave at 1.35 V (Fig. 7b). The reversible redox wave at 0.86 V corresponds to the first oxidation wave observed when 300 mM water is added to the **NiL1** solution, suggesting the formation of the Ni(II)/Ni(III) species at this oxidation step. The second redox peak was attributed to ligand-based oxidation. To further evaluate the redox properties associated with ligand-based oxidation, we synthesized an analogous Zn(II) complex of **L1** ligand. ^{1}H NMR (Fig. S19a and b) and HR-MS (Fig. S19c and d) analyses suggested that Zn(II) coordinates differently. It binds the $\mathbf{H_2L1}$ ligand in a tridentate fashion. Earlier, we have reported a similar structure for the Cu(II) complex of $\mathbf{H_2L1}$.[28b] The CV of the Zn complex supports that the second oxidation wave in the Ni(II) complex arises from the ligand-based oxidation as Zn(II) is redox inactive under these conditions (Fig. S19e and f).

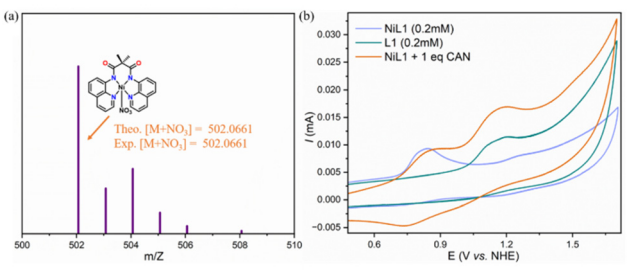

Fig. 7 (a) HRMS spectrum of **NiL1** with 1 equiv. of CAN added to it (observed *m/z* [$C_{23}H_{18}N_4NiO_2$ + NO_3]: 502.0661, theoretical *m/z*: 502.0661). (b) CV response when 1 equivalent of CAN was added to **NiL1** (0.2 mM).

Pourbaix diagram

The stability of different redox states of **NiL*X*** complexes (X = 1, 2, 3) across various pH values was determined using a Pourbaix diagram and cyclic voltammetry. The experiments were conducted in a 0.1 M phosphate buffer solution at pH levels ranging from 6 to 9, with 0.2 mM Ni(II) complexes added to the solution. A glassy carbon (GC) electrode was used as the working electrode to study the electrochemical behaviour of all complexes at different pH levels. It was observed that the electrochemical behaviour remained consistent across the pH range of 6–9 (Fig. 7). The first oxidation wave for the three complexes occurred at potentials of 0.78 V, 0.82 V, and 0.87 V, respectively, and this step was found to be pH-dependent. The peak potential gradually decreased as the pH increased, with a slope of 54 mV pH^{-1} for **NiL1**, 55 mV pH^{-1} for **NiL2**, and 50 mV pH^{-1} for **NiL3** (Fig. 8 and Fig. S20 for **NiL1**; Fig. S21–S24 for **NiL2** and **NiL3**). These slope values suggest a proton-coupled electron transfer (PCET) process (**Ni(II)L1** + H_2O → **Ni(III)L1(OH)** + H^+). The second oxidation wave was observed at 1.32 V, 1.31 V, and 1.28 V for **NiL1**, **NiL2**, and **NiL3**, respectively. This second peak was pH-independent in all cases and

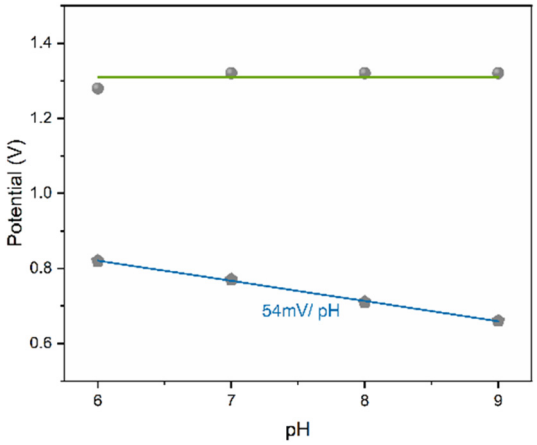

Fig. 8 Pourbaix diagram (plot of potential of two oxidation peaks *vs.* pH) for complex **NiL1** (0.2 mM) in 0.1 M PBS using glassy carbon as the working electrode and Pt wire as the counter electrode.

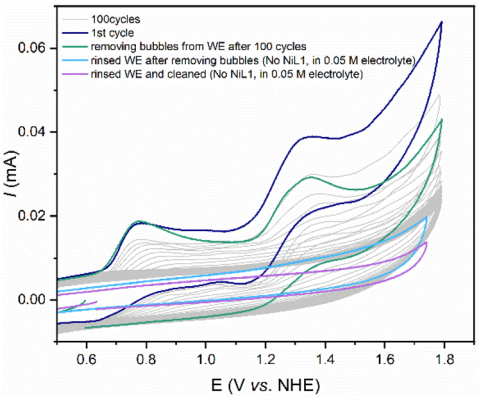

Fig. 9 Consecutive 100 CV scans of **NiL1** (0.2 mM) in 0.05 M $^{n}Bu_4NPF_6$/ACN dissolved as a supporting electrolyte at scan rate = 100 mV s^{-1} and 300 mM water added to it using GC as the working electrode (WE).

corresponds to ligand-based oxidation (**Ni(III)L1(OH)** → **Ni(III)L1$^{\bullet+}$(OH)** + e).

Evidence for homogeneity

There are very few examples in the literature of Ni(II)-catalysed homogeneous water oxidation. In most of the cases, NiO_x or NiOOH species are deposited on the electrode and become the active catalyst. In the literature, several factors provide evidence for the involvement of a heterogeneous catalyst.[32] These include the crossover observed in cyclic voltammetry (CV) and a non-linear relationship between concentration and catalytic current. Other indicators are the consistent catalytic activity under identical conditions for the attributed metal ion and the increase in current over successive CV cycles. Additionally, differences in UV-Vis spectra before and after electrolysis, as well as the catalytic current detected at the anode in a fresh electrolyte after electrolysis, further support the absence of heterogeneous catalysis.

To check the homogeneity of the molecular Ni(II) catalyst, a CV experiment was performed with 100 cycles between 0.5 and 1.8 V *vs.* NHE in a 0.2 mM Ni(L) complex and 0.05 M ($^{n}Bu_4NPF_6$) supporting electrolyte solution, in the presence of 300 mM water (total volume 10 mL). The catalytic current decreased after multiple scans. After 100 cycles, bubbles were removed from the GC electrode, and a CV experiment was performed in the same solution. Both the redox peaks were visible. The electrode was then rinsed with acetonitrile to remove any remaining complex. Subsequently, a CV experiment was performed using the same rinsed electrode in 0.05 M $^{n}Bu_4NPF_6$ solution. A slightly higher current was observed compared to the current recorded in the blank, where the electrode was rinsed and polished with alumina powder. However, this increase in current is lower than the catalytic current of 17.5 μA observed in the presence of the **NiL1** complex in the solution (Fig. 9 and Fig. S25 for **NiL2** and **NiL3**). Then, a controlled potential experiment (CPE) was conducted for two hours using fluorine-doped tin oxide (FTO) as the working electrode to check the stability of the catalyst **NiL1**. After completion of the experiment, the electrode was washed properly, and FE-SEM and EDX analyses were carried out. The analyses of the electrode before and after the CPE are compared in Fig. S26. No evidence was found for NiO_x deposition on the electrode surface. The electronic absorption spectra of the catalysts before and after bulk electrolysis remain the same, indicating the overall stability of the complexes during the oxidation process (Fig. S27). Furthermore, we performed X-ray photoelectron spectroscopy (XPS) of the FTO electrode after bulk electrolysis, and no evidence of NiO_x formation was observed (Fig. S28).

Kinetic analysis

To elucidate the mechanism of water oxidation catalyzed by Ni(II) complexes (**NiL1**, **NiL2**, and **NiL3**), kinetic studies were performed. The catalytic rate constant (k_{cat}) was determined by comparing the i_{cat}/i_p against $\nu^{-1/2}$ using eqn (4) (Fig. 10, Fig. S29–30 and Table 2). Similarly, from the scan rate-dependent study, the rate constant (k_0) was also determined by plotting i_{cat}/i_p against $\nu^{-1/2}$ for all three complexes according to eqn (5) (Fig. 10b). The k_0 values were calculated to be 1.42 M^{-1} s^{-1}, 1.05 M^{-1} s^{-1}, and 1.99 M^{-1} s^{-1} for **NiL1**, **NiL2**, and **NiL3**, respectively.

$$\frac{i_{cat}}{i_p} = 2.242\left(\frac{k_{cat}RT}{nF\nu}\right)^{1/2} \quad (4)$$

$$\frac{i_{cat}}{i_p} = 2.242\left(\frac{k_0RT[H_2O]}{nF\nu}\right)^{1/2} \quad (5)$$

To determine the kinetic isotope effect (KIE), experiments were conducted using D_2O as the substrate instead of H_2O. A decrease of 2 μA in catalytic current was observed when cyclic voltammetry (CV) measurements were performed in the presence of D_2O (Fig. 10a). While the catalytic potential for the first oxidation event remained unchanged, the CV showed a

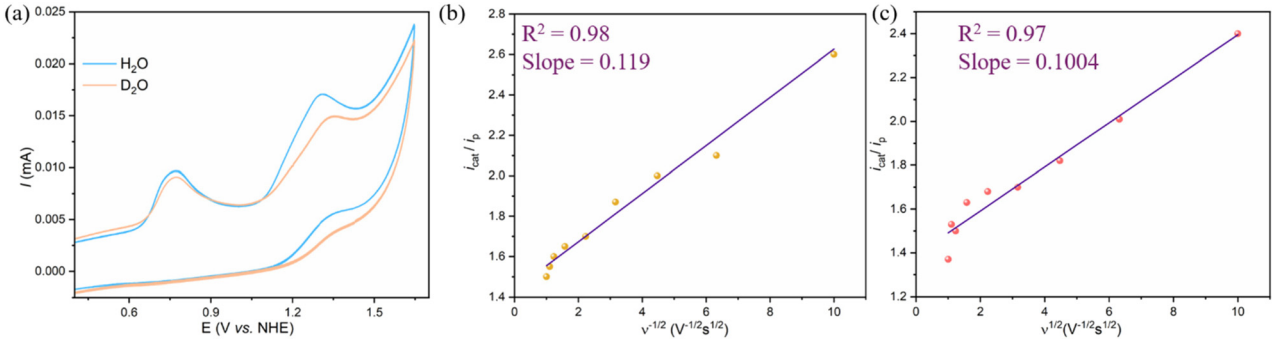

Fig. 10 (a) CVs of **NiL1** (0.2 mM) with added 300 mM H_2O (blue) and D_2O (orange) (scan rate: 100 mV s^{-1}). (b) Plot of i_{cat}/i_p as a function of the inverse of the square root of scan rate in the case of H_2O for **NiL1**. (c) Plot of i_{cat}/i_p as a function of the inverse of the square root of scan rate in the case of D_2O for **NiL1**.

Table 2 Comprehensive evaluation of catalytic performances calculated from electrochemical studies

Catalyst	k_{cat,H_2O} (M^{-1} s^{-1})	k_{cat,D_2O} (M^{-1} s^{-1})	Faradaic efficiency (%)	KIE
NiL1	1.42	1.01	94.6	1.41
NiL2	1.05	0.915	86.14	1.15
NiL3	1.99	1.6	99.04	1.24

40 mV positive shift in the peak potential for the ligand-based oxidation event. The catalytic rate constant (k_{cat}) for the **NiL1** complex in D_2O was estimated to be 1.01 M^{-1} s^{-1} (Fig. 10c). The KIE was calculated by taking the ratio of the rate constants k_{H_2O} and k_{D_2O} using eqn (6), measured in H_2O and D_2O, respectively. The KIE values for **NiL1**, **NiL2**, and **NiL3** were found to be 1.41, 1.15, and 1.24, respectively.

$$\frac{k_{cat,H_2O}}{k_{cat,D_2O}} = \left(\frac{i_{cat,H_2O}}{k_{cat,D_2O}}\right)^2 \quad (6)$$

The KIE value of ≤1.42 observed in our case matches the value reported by Meyer and co-workers for water oxidation using the $[Ru^{II}(Mebimpy)(bpy)(OH_2)]^{2+}$ [Mebimpy = 2,6-bis(1-methylbenzimidazol-2-yl)pyridine; bpy = 2,2′-bipyridine] complex.[33] They observed involvement of a single water molecule in the rate law and a direct O-atom transfer, leading to a coordinated hydrogen peroxide intermediate. A similar observation was found for an Fe^{III}-aqua complex ($[Fe^{III}(dpaq)(H_2O)]^{2+}$), where the formation of the peroxide (O–O) bond was the rate-limiting step (KIE value 1.08).[34] Therefore, a first order reaction in [H_2O] and the absence of a significant KIE point to a mechanism involving O–O bond formation to generate the peroxide intermediate. However, in the case of $[Ru^{V}(tpy)(bpm)(O)]^{3+}$ (where tpy is 2,2′:6′,2″-terpyridine and bpm is 2,2′-bipyrimidine), the KIE value reaches approximately 6.6 when H_2O is used as the base.[35] This higher KIE value has been attributed to the atom-proton transfer (APT) in the rate-determining O–O bond formation step.

Bulk electrolysis and oxygen detection

To evaluate the catalytic activity of Ni(II) complexes, long-term bulk electrolysis experiments (3 h) were conducted at 1.3 V (for **NiL1**), 1.2 V (for **NiL2**) and 1.45 V (for **NiL3**), respectively, using FTO (1 cm × 1 cm) as the working electrode, both in the presence and absence (blank) of the catalyst. The experiment was carried out in a customised H-type cell containing 0.2 mM Ni(II) complexes in a 0.05 M $^nBu_4PF_6$/ACN solution, and 1000 mM water was added to it. During bulk electrolysis, the background current in the absence of a catalyst was negligibly small, as indicated by the black line in Fig. 11. In contrast, a sustained current of 50 μA cm^{-2} was observed throughout the electrolysis of complex **NiL1** (Fig. 11a). During electrolysis, oxygen bubbles consistently formed at the electrode surface, and O_2 formed in the headspace was analysed using gas chromatography equipped with a thermal conductivity detector (GC-TCD) (Fig. S31a: calibration curve). After 3 h of electrolysis at 1.3 V, ~4.24 μmol of O_2 was analysed, corresponding to a faradaic efficiency of 94.6%, for **NiL1** (Table S4). Additionally, bulk electrolysis experiments of **NiL2** and **NiL3** showed that the values of O_2 detected were 3.12 μmol and 9.35 μmol, which correspond to faradaic efficiencies of 86.14% and 99.04%, respectively (Table 2). Turnover numbers (TONs) of **NiL1**, **NiL2**, and **NiL3** are determined to be 7.29, 5.86, and 16.4, respectively. However, since only the catalyst present in the layer of the solution in contact with the electrode is involved in the water oxidation reaction, this TON value is underestimated. Details of the calculation of TONs are provided in the SI. O_2 was not detected when CPE was carried out in the presence of **ZnL1** with water. The current density *vs.* reaction time plot of bulk electrolysis for **ZnL1** is given in Fig. S31b.

The direct application of the Randles–Ševčík method for TOF determination can lead to an overestimation of the TOF and potentially obscure the actual kinetic behaviour of the system. In contrast, foot-of-the-wave analysis (FOWA) proposed by Costentin and Savéant[36] offers a clearer representation of the kinetics involved in this multi-electron oxygen evolution reaction (OER) catalyzed by Ni(II) amido-quinoline complexes. Typically expressed by eqn (7), FOWA enables a more practical

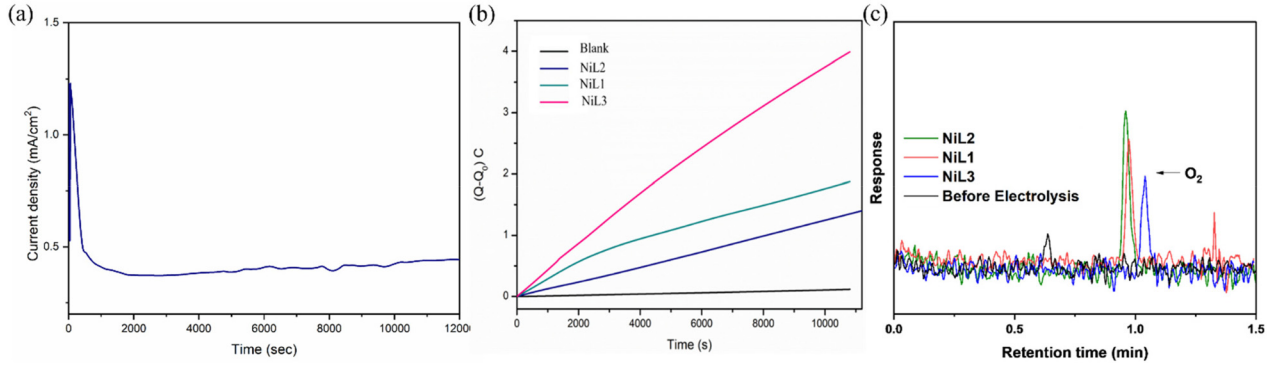

Fig. 11 (a) Plot of current density *vs.* reaction time during bulk electrolysis of complex **NiL1** (0.2 mM) at 1.3 V using FTO as the working electrode. (b) Charge *vs.* time plots from CPE performed at catalytic peak potentials over 60 minutes. Solutions contain 0.05 M $^{n}Bu_4NPF_6$ and 300 mM H_2O in acetonitrile with added 0.1 mM **NiL1** (red, 1.35 V), 0.1 mM **NiL2** (green, 1.2 V), and 0.1 mM **NiL3** (blue, 1.45 V). The control experiment (black) was conducted at 1.45 V *vs.* Ag/$AgNO_3$ with a freshly prepared identical solution, except that no catalyst (black) was added. (c) O_2 evolution measured by GC-TCD during CPE in 0.05 M $^{n}Bu_4NPF_6$ of 0.2 mM Ni(II) complexes.

evaluation by allowing the extraction of kinetic parameters in a straightforward manner, free from the complications introduced by diffusion limitations and nonlinear effects. The pseudo first order rate constant [k (or TOF)] was determined from the slope (m) of the linear plot of i_{cat}/i_p *vs.* $1/(1 + e^{F(E_{cat/2}-E)/RT})$ (eqn (7)). The estimated rate constants or TOFs are 1.98 s^{-1}, 0.96 s^{-1}, and 3.89 s^{-1}, respectively, for **NiL1**, **NiL2**, and **NiL3** according to eqn (9) (Fig. S32).

$$\frac{i_{cat}}{i_p} = \frac{4 \times 2.24 \times \sqrt{\frac{RTk_{obs}}{Fv}}}{1 + \exp\left\{\frac{F}{RT}(E_{cat/2} - E)\right\}} \quad (7)$$

$$m = 4 \times 2.24 \times \sqrt{\frac{RTk_{obs}}{Fv}} \quad (8)$$

$$\mathrm{TOF} = m^2 \times \left[\frac{Fv}{RT} \times (4 \times 2.24)^2\right] \quad (9)$$

A controlled potential electrolysis was performed using $H_2{}^{18}O$ along with $H_2{}^{16}O$ under our standard catalytic conditions (150 mm $H_2{}^{18}O$; 150 mM $H_2{}^{16}O$ with 0.05 M $^{n}Bu_4NPF_6$ as a supporting electrolyte). Upon analysis by GC-MS, a signal of molecular mass 36 ($^{18}O_2$) along with a molecular mass 34 (may be a combination of ^{16}O and ^{18}O) was observed. These data further support that the evolved O_2 originates from water oxidation (Fig. S33).

Mechanism: effect of the ligand framework on water oxidation

Based on the experimental findings from the spectroelectrochemical experiment, the effect of pH on redox potential, the KIE and homogeneity of solution during the electrochemical experiment, we proposed a mechanism for water oxidation by the Ni(II) complexes containing amido-quinoline ligands, as outlined in Fig. 12. The mechanism starts with the reaction of [Ni(II)L] (**int1**) through a proton coupled electron transfer (PCET) process. In the next step, one-electron oxidation of the ligand framework (redox-active amido-quinoline) leads to **int3**.[37] The oxidized [Ni(III)L-OH] could form **int4** [NiL-O$^{\bullet}$] *via* a proton transfer step. [NiL-O$^{\bullet}$] could allow the evolution of O_2 *via* catalytic pathways I (path I) or II (path II). In path I, **int4** could undergo another PCET reaction with the water molecule, forming a peroxy intermediate [NiL-OOH] (**int5**). Alternatively, *via* path II, **int4** could react with the water molecule and form [NiL(OH)O$^{\bullet}$] (**int4a**). **Int4** could also generate NiL-OOH (**int5**) *via* an electrochemical ($\Delta G_{4'}$) and thermal recombination step ($\Delta G_{5'}$). NiL-OOH will undergo a PCET step in the final step to evolve the O_2 and the catalytic site (**intI**).

To understand the feasible catalytic pathway between path I and II, density functional theory (DFT) calculations were performed.[37–39]

The most stable spin states were determined for the catalysts and were considered to calculate the binding energies of the reaction intermediates. The DFT-optimized structures for **NiL1**, **NiL2**, and **NiL3** complexes in singlet spin as a ground state are provided in Fig. S34. The reaction free energy diagrams for both paths at an applied potential of 1.3 V and pH 7 are shown in Fig. 13. The formation of [NiL-OH], **int2**, was exothermic for all three complexes. Ni(II)L1 showed the highest exothermicity, whereas Ni(II)L3 showed the lowest exothermicity. The ligand oxidation step showed a similar trend (−1.2 eV for **NiL1**, −1.2 eV for **NiL2**, and −1.12 eV for **NiL3**). The increment in the bond length of the aromatic ring in **int3** confirms the oxidation of the ligand framework. The structural parameters before and after ligand oxidation are provided in Fig. S35. We performed natural bond orbital (NBO) analysis to quantify the charge distributions during the oxidation process of the ligand (Table S5). The oxidation of the amido-quinoline ligand is clearly indicated by the NBO charges. The ligand partial charge densities of [NiL-OH] and [NiL$^{\bullet+}$-OH] intermediates increase in the range from 0.98 to 1.00 during this oxidation process.

Path I corresponds to the traditional water oxidation mechanism (WNA). In this pathway, for all **NiL*X*** complexes,

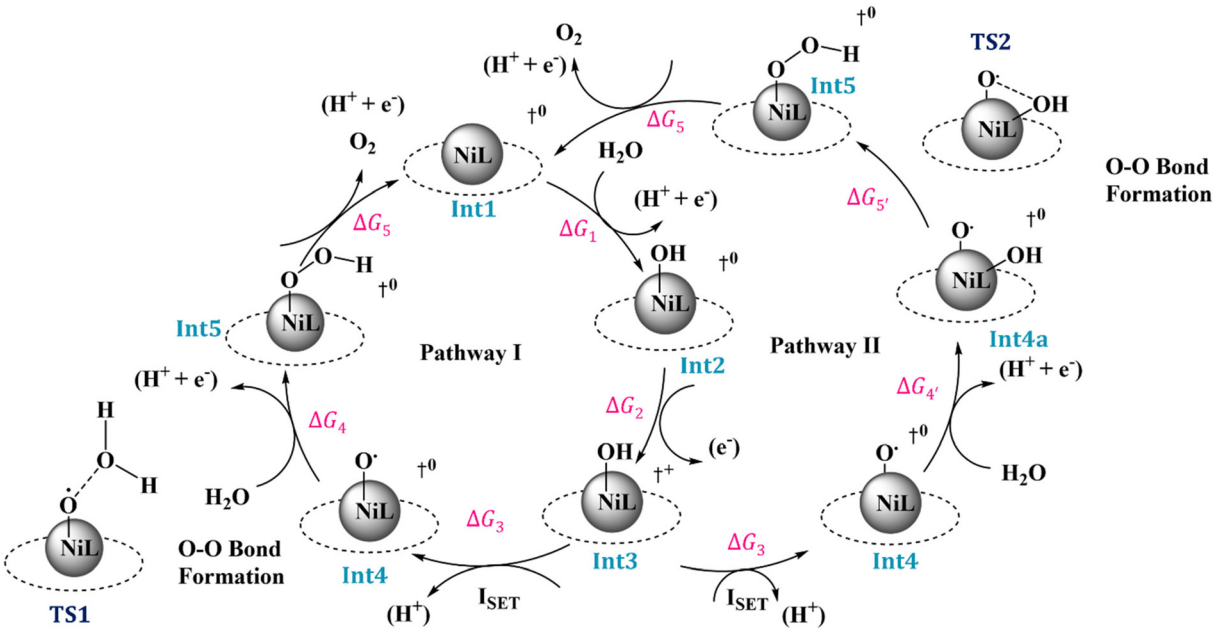

Fig. 12 The proposed mechanistic pathway for water oxidation using the amido quinoline-based nickel catalyst. The overall complex and intermediate charges are shown along the reaction pathway.

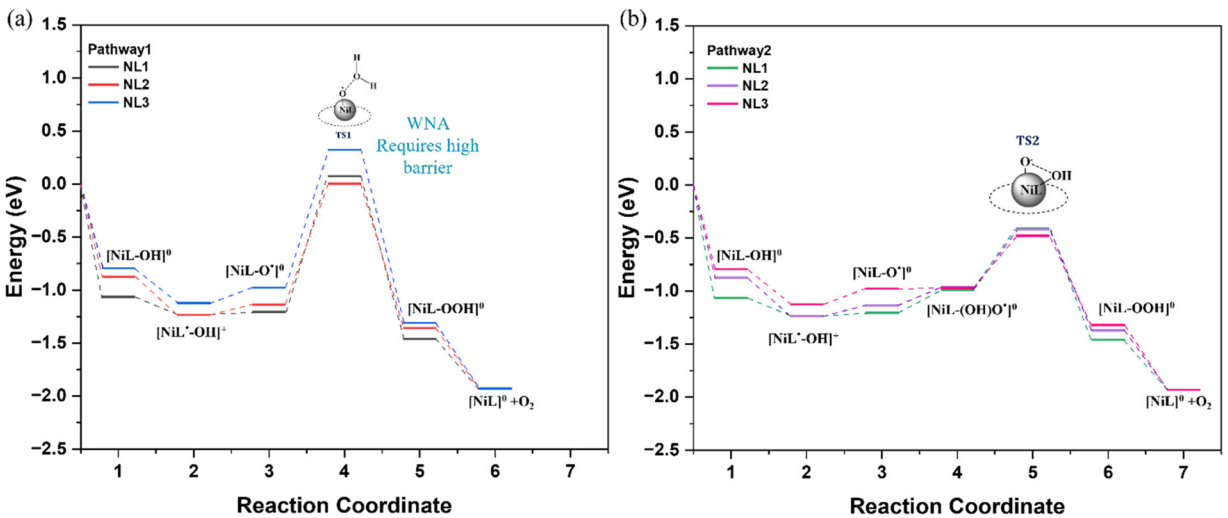

Fig. 13 Free energy diagram (applied potential: 1.3 V) for the water oxidation catalyst. (a) Water nucleophilic pathway I (WNA); (b) alternative intramolecular oxygen HO–O coupling pathway II.

the formation of **int4**, [Ni(III)L-O$^{\bullet}$], is slightly endothermic, varying in the range from 0.03 to 0.15 eV (Fig. 13a). The NBO spin density calculation suggests that the observed Ni oxo spices have radical behaviour with the unpaired electron on the oxygen atom (Table S6). However, we observed a high kinetic (1.1 to 1.3 eV) barrier for forming a peroxo intermediate, [Ni(III)L-OOH] (**int5**) from [Ni(III)L-O$^{\bullet}$]. This step corresponds to the rate-determining (RDS) step in this pathway.

Alternatively, in path II (Fig. 13b), the associated reaction free energies follow the same energy profile as in path I up to the formation of **int4**. In path II, the formation of [NiL(OH)(O$^{\bullet}$)] from the [NiLO$^{\bullet}$] intermediate is the potential-determining step (PDS), whereas thermal recombination *via* intramolecular O–O coupling from [NiL(OH)(O$^{\bullet}$)] (**int4a**) to form [NiL-OOH] (**int5**) corresponds to the RDS. The kinetic barrier (ranging between 0.49 and 0.58 eV for the **NiL*X*** complexes) for the coupling step was lower than the kinetic barrier obtained for [NiL-OOH] formation in path I. These values indicate that path II would be more favourable than path I.

The calculated transition state for the intramolecular O–O coupling among the different **NiL*X*** complexes in path II follows the trend of **NiL3** < **NiL1**~**NiL2**. Therefore, **NiL3** would

have greater catalytic activity than **NiL1** and **NiL2**. This greatly corresponds with the experimental results. Comparing the thermodynamic barriers for the formation of **int5a** in **NiL1** and **NiL2**, **NiL1** showed slightly higher exothermicity than **NiL2** (−1.46 eV for **NiL1** and −1.37 eV for **NiL2**). An increment in the TOF for **NiL1** compared to **NiL2** was observed during the experiments. The evolution of an oxygen molecule from [NiL-OOH] through the PCET process is exothermic, ranging between −0.4 and −0.6 eV.

It is to be noted that among the three complexes, **NiL3** shows the least thermodynamic stability for most of the intermediates. The lower stability of [NiL(OH)(O$^{\bullet}$)] for **NiL3** reduces the thermodynamic barrier for [NiL-OOH] formation. To understand the electronic effects of the Ni amido quinoline catalyst on the kinetic activity of the water oxidation reaction, we calculated the spin density of the [NiL(OH)(O$^{\bullet}$)] intermediate (**int4a**). The spin density values are provided in Table S6. The spin density values contribute to electron density on the O atom following the trend: **NiL3** < **NiL1** < **NiL2**. The spin density reduces the reactivity of the O radical on the **NiL3** complex compared to that on the **NiL1** complex.

The phenyl ring in the **NiL3** complex acts as an electron-withdrawing group, whereas the –CMe$_2$ and –NMe groups in **NiL2** and **NiL1** increase the electron density. The NBO charge density analysis of the potential reactive species (**Ni–O$^{\bullet}$**) was performed to justify the statement (Table S7). The charge density calculations show the following trend for the partial positive charge on the metal atom: **NiL3** > **NiL1** > **NiL2**. The electron-withdrawing nature of –CPh reduces the electron density of the **NiL3** complex marginally in comparison with **NiL2** and **NiL1** complexes. The marginal differences in the spin density of the active metal center bring in marginal differences in the activity. In previous studies, it has been shown that an electron-withdrawing group surrounding the oxyl radical can reduce the kinetic barrier of the water oxidation reaction to an electron-releasing group.[38,39]

The proximity of the hydrogen (adjacent to the attached phenyl group) in the optimized **Ni–O$^{\bullet}$** intermediate structure of the **NiL3** complex (approximately 2.6 Å away from the H of the Ph–C–H moiety) led us to investigate an alternative reaction pathway. In this mechanism, we explored the possibility of proton abstraction from the Ph–CH moiety of the **NiL3** complex *via* the radical pathway. Fig. S36 in the SI shows the possible reaction pathway. Proton abstraction was found to have an energy barrier of 8 kcal mol^{-1}. Following the proton abstraction, one of the reaction steps is found to have much higher endothermicity than path II. Therefore, we disregarded the feasibility of this pathway for the O_2 evolution on the **NiL3** complex.

Experimental

Materials and methods

All chemicals and reagents were used as received from commercial sources without any further purification. Phenyl malonic acid was purchased from TCI Chemicals. Sodium sulfite and dimethyl malonyl chloride were purchased from Sigma Aldrich. $NiCl_2{\cdot}6H_2O$ was purchased from BLD Pharma. All the solvents used during the synthesis and analysis were of HPLC grade and were distilled prior to use according to standard procedures. Milli-Q distilled water was used during the oxidation process. $^{n}Bu_4NPF_6$ was recrystallized prior to the use and was used as a supporting electrolyte for the electrochemical tests. The single-crystal X-ray data of all the nickel complexes were obtained through the measurement of X-ray diffraction data on a D8 Venture Bruker AXS single-crystal X-ray diffractometer. This diffractometer is equipped with a CMOS PHOTON 100 detector, which has monochromatized microfocus sources (Mo-Kα = 0.71073 Å). A Jeol JSM-7610Plus model field-emission scanning electron microscope (FE-SEM) equipped with energy-dispersive X-ray analysis (EDX) was used to study the surface morphology of electrodes. All the electrochemical analyses were performed using a Biologic, SP-300 electrochemical workstation through cyclic voltammetry (CV), differential pulse voltammetry (DPV), and chronoamperometry (CA) measurements in an ACN medium ([Ni(II)L1/2/3] = 0.2 mM) at a scan rate of 0.1 V s^{-1}. The supporting electrolyte used during the analysis was 0.05 M $^{n}Bu_4NPF_6$ (^{n}Bu = *n*-butyl). UV-vis spectral studies were carried out on an Agilent diode array Cary 8454 spectrophotometer, ranging from 190 nm to 1100 nm in quartz cuvettes. All ^{1}H and ^{13}C NMR spectra were recorded using a Bruker 400 MHz instrument at 400 MHz for ^{1}H and 100 MHz for ^{13}C NMR spectroscopy, taking tetramethylsilane (TMS) as an internal standard at room temperature. High-resolution mass spectroscopy (HRMS) analysis was performed using a 6540 UHD Accurate-Mass Q-TOF LC/MS system (Agilent Technologies, Santa Clara, CA, USA) equipped with an Agilent 1290 ultra-performance liquid chromatography (UPLC) system. Mass spectra were obtained in the positive-ion mode ranging from 100 to 1500 mass-to-charge ratio (*m*/*z*). The mobile phase composition consisted of H_2O (A) and ACN (B), with optimized linear gradient elution with an injection volume of 5 μL and a flow rate of 0.3 mL min^{-1}. Elemental analysis was carried out with a PerkinElmer CHN analyzer (2400 series). The X-ray photoelectron spectroscopy (XPS) spectrum was recorded with a Thermo Fisher Scientific system with micro-focused X-ray (400 μm spot size, 72 W, 12 000 V) monochromatic AI-Kα source ($h\nu$ = 1486.6 eV), a hemispherical analyser, and a 128-channel plate detector. Taking the maximum intensity of the C 1s signal at 284.8 eV as the reference, the binding energies were calculated.

Crystallographic studies

Data collection of Ni(II) complexes was performed by choosing a single crystal of suitable dimensions. Single crystals of complex **3** suitable for X-ray diffraction data collection were obtained by slow evaporation from DCM/diethyl ether solution, whereas for complexes **1** and **2**, single crystals were obtained from DMF solution. Diffraction data were collected on a D8 Venture Bruker AXS single crystal X-ray diffractometer equipped with a CMOS PHOTON 100 detector having monochromatised microfocus sources (Mo-Kα = 0.71073 Å). Data collection was performed at room temperature, and structures were solved using APEX3 refined on F2 by using all data by

full-matrix least-squares procedures with SHELXL-2016 and incorporated into the olex2-1.5 Package.[40–42] The hydrogen atoms were placed at the calculated positions and included in the last cycles of the refinement. All crystal structures are represented with the MERCURY program.[43]

Electrochemical measurements

Experiments were performed in a standard three-electrode system and were conducted in a 5 mL electrochemical cell with a Teflon cap under ambient conditions. Electrochemical analyses were recorded in acetonitrile using glassy carbon as the working electrode (0.07 cm^2), a platinum wire as the counter electrode and the $Ag/AgNO_3$ electrode (0.01 M $AgNO_3$, 0.1 M $^nBu_4NPF_6$ in acetonitrile) as the reference electrode with potentials reported *vs*. the normal hydrogen electrode (NHE) by the subtraction of 0.354 V from the measured potentials. Before each scan in CV, the glassy carbon was thoroughly cleaned using micropolish powder of alumina suspension (size 0.05 micron). In the bulk electrolysis experiment, the electrochemical cell was tightly sealed with septum caps, and the cell was degassed with Ar gas for 30 minutes before starting the bulk electrolysis experiment. A fluorine-doped tin oxide (FTO) electrode was employed as the working electrode, while an $Ag/AgNO_3$ electrode (0.01 M $AgNO_3$, 0.1 M $^nBu_4NPF_6$ in acetonitrile) was used as the reference electrode and a platinum wire was chosen as the counter electrode. The amount of oxygen that evolved during water oxidation was monitored by gas chromatography. O_2 detection was performed using an Agilent 8860 GC instrument with a thermal conductivity detector (TCD). The experiment was conducted under continuous stirring, and 100 μL of gas was taken from the headspace of the cell using a gastight luer-lock Hamilton syringe. The GC setup utilized a Molsieve 5 Å column using N_2 as the carrier gas and the column temperature was maintained at 100 °C. A control experiment was carried out under similar conditions in the absence of Ni(II) complexes.

Spectroelectrochemical study

An Ocean insight DH-2000-BAL UV-Vis NIR light source was used for the spectro-electrochemistry experiment. A Gamry interface 1000 series potentiostat was used to apply the constant potential. The spectroelectrochemical data were recorded in a 3 ml quartz cuvette with a 1 cm path length. The cuvette holder was connected to the light source and the detector through optical fibre cables. A platinum mesh electrode was used as the working electrode, an $Ag/AgNO_3$ electrode as the reference electrode, and another platinum wire was used as the counter electrode. The potential was held at 0.78 *vs*. NHE for 30 minutes. Time-dependent UV-visible spectral change was recorded at intervals of 1 minute.

Conclusion

In summary, Ni(II) amido-quinoline complexes (**NiL1**, **NiL2**, and **NiL3**) were synthesized and examined as molecular water oxidation catalysts in a non-aqueous medium where water was used as the limiting reagent. Field emission scanning electron microscopy (FE-SEM) and energy-dispersive X-ray spectroscopy (EDX) revealed no evidence of NiO_x film deposition on the working electrode surface. For all three complexes, we proposed the formation of energetically favorable radical intermediates whose electronic structures were obtained by spin density calculations in DFT. The participation of the redox-active ligands facilitates the delocalization of an electron in the π system of the ligand. It helps escape the increasing oxidation state of the Ni^{III} center to the higher oxidation states during the oxidation process. KIE analysis suggested the formation of a peroxo intermediate as the rate-determining step. The DFT calculations show that Ni amido quinoline complexes do not follow the traditional water oxidation mechanism. The coupling of Ni–O$^\bullet$ and OH$^\bullet$ intermediates was found to have a lower kinetic barrier compared to the electrochemical oxidation of the Ni–O$^\bullet$ intermediate with water, involving a proton-coupled electron transfer step. The thermodynamic calculations using DFT show that the reaction proceeds *via* a radical pathway, where the coupling of Ni–O$^\bullet$ and the adsorbed OH intermediate allows the formation of the NiL-OOH intermediate. The electrochemical oxidation of Ni–O$^\bullet$ with a water molecule involving a proton-coupled electron transfer step was less favourable. Further studies are ongoing to optimize the ligand backbone by introducing various substituents and functional groups, with the aim of developing more efficient molecular catalysts with enhanced performance.

Author contributions

Monika and BBD conceptualized the work. All the synthesis, characterisation, and electrochemical analyses were performed by Monika. Theoretical calculations were performed by VM and NK. The manuscript was written by Monika and BBD with the help of all the co-authors. The spectroelectrochemical experiment was performed by PK.

Conflicts of interest

There are no conflicts to declare.

Data availability

The data supporting this article have been included as part of the supplementary information (SI). Supplementary information is available. Experimental and DFT calculations, synthesis, characterization, supplementary spectroscopic, electrochemical, and structural data information. See DOI: **https://doi.org/10.1039/d5qi02127h**.

CCDC 2419464 and 2444267 contain the supplementary crystallographic data for this paper.[44a,b]

Acknowledgements

BBD acknowledges CSIR and SERB, DST, New Delhi (Grant no. EMR-II 80(0086)/17; CRG/2022/001576), for funding. Monika and VM acknowledge SNIoE and Shiv Nadar Foundation for a fellowship and computational support (High-performance computing system MAGUS). Monika and VM acknowledge CSIR for providing a senior research fellowship. NK acknowledges SNIoE for computational support and funding. All the authors are thankful to Dr Santanu Pattanayak for helping with electrochemical analysis.

References

1 N. S. Lewis and D. G. Nocera, Powering the planet: chemical challenges in solar energy utilization, *Proc. Natl. Acad. Sci. U. S. A.*, 2006, **103**, 15729–15735.
2 B. Zhang and L. Sun, Artificial photosynthesis: opportunities and challenges of molecular catalysts, *Chem. Soc. Rev.*, 2019, **48**, 2216–2264.
3 M. Suga, F. Akita, K. Yamashita, Y. Nakajima, G. Ueno, H. Li, T. Yamane, K. Hirata, Y. Umena, S. Yonekura, L.-J. Yu, H. Murakami, T. Nomura, T. Kimura, M. Kubo, S. Baba, T. Kumasaka, K. Tono, M. Yabashi, H. Isobe, K. Yamaguchi, M. Yamamoto, H. Ago and J.-R. Shen, An oxyl/oxo mechanism for oxygen-oxygen coupling in PSII revealed by an X-Ray free-electron laser, *Science*, 2019, **366**, 334–338.
4 Y. Umena, K. Kawakami, J.-R. Shen and N. Kamiya, Crystal structure of oxygen-evolving Photosystem II at a resolution of 1. 9 Å, *Nature*, 2011, **473**, 55–60.
5 J. S. Kanady, E. Y. Tsui, M. W. Day and T. Agapie, A synthetic model of the Mn3Ca subsite of the oxygen-evolving complex in Photosystem II, *Science*, 2011, **333**, 733–736.
6 J. D. Blakemore, R. H. Crabtree and G. W. Brudvig, Molecular catalysts for water oxidation, *Chem. Rev.*, 2015, **115**, 12974–13005.
7 B. M. Hunter, H. B. Gray and A. M. Müller, Earth-abundant heterogeneous water oxidation catalysts, *Chem. Rev.*, 2016, **116**, 14120–14136.
8 S. W. Gersten, G. J. Samuels and T. J. Meyer, Catalytic oxidation of water by an oxo-bridged ruthenium dimer, *J. Am. Chem. Soc.*, 1982, **104**, 4029–4030.
9 (*a*) T. Liu and L. Sun, Proton transfer regulating in catalytic water oxidation by Ru-complexes: second coordination sphere and beyond, *Sci. Bull.*, 2023, **68**, 854–856; (*b*) Y. Xu, T. Akermark, V. Gyollai, D. Zou, L. Eriksson, L. Duan, R. Zhang, B. Akermark and L. Sun, A New dinuclear ruthenium complex as an efficient water oxidation catalyst, *Inorg. Chem.*, 2009, **48**, 2717–2719.
10 J. F. Hull, D. Balcells, J. D. Blakemore, C. D. Incarvito, O. Eisenstein, G. W. Brudvig and R. H. Crabtree, Highly active and robust Cp* iridium complexes for catalytic water oxidation, *J. Am. Chem. Soc.*, 2009, **131**, 8730–8731.
11 K. S. Joya, N. K. Subbaiyan, F. D'Souza and H. J. M. de Groot, Surface-immobilized single-site iridium complexes for electrocatalytic water splitting, *Angew. Chem., Int. Ed.*, 2012, **51**, 9601–9605.
12 A. Akbari, M. Amini, A. Tarassoli, B. Eftekhari-Sis, N. Ghasemianand and E. Jabbari, Transition metal oxide nanoparticles as efficient catalysts in oxidation reactions, *Nano-Struct. Nano-Objects*, 2018, **14**, 19–48.
13 Y. Shimazaki, T. Nagano, H. Takesue, B. Ye, F. Tani and Y. Naruta, Characterization of a dinuclear MnV = O complex and is efficient evolution of O_2 in the presence of water, *Angew. Chem., Int. Ed.*, 2004, **43**, 98–100.
14 K. J. Young, M. K. Takase and G. W. Brudvig, An anionic N-donor ligand promotes manganese-catalyzed water oxidation, *Inorg. Chem.*, 2013, **52**, 7615–7622.
15 H.-T. Zhang, X.-J. Su, F. Xie, R.-Z. Liao and M.-T. Zhang, Iron-catalyzed water oxidation: O–O bond formation via intramolecular oxo–oxo interaction, *Angew. Chem., Int. Ed.*, 2021, **60**, 12467–12474.
16 W. Sinha, A. Mahammed, N. Fridman and Z. Gross, Water oxidation catalysis by mono- and binuclear iron corroles, *ACS Catal.*, 2020, **10**, 3764–3772.
17 B. Mondal, S. Chattopadhyay, S. Dey, A. Mahammed, K. Mittra, A. Rana, Z. Gross and A. Dey, Elucidation of factors that govern the 2e−/2H+ vs 4e−/4H+ selectivity of water oxidation by a cobalt corrole, *J. Am. Chem. Soc.*, 2020, **142**, 21040–21049.
18 D. D. Boer, Q. Siberie, M. A. Siegler, T. H. Ferber, D. C. Moritz, J. P. Hoffman and D. G. H. Hetterscheid, On the homogeneity of a cobalt-based water oxidation catalyst, *ACS Catal.*, 2022, **12**, 4597–4607.
19 J. W. Wang, C. Hou, H. H. Huang, L. Sun, W. J. Liu, Z. F. Ke and T. B. Lu, Further insight into the electrocatalytic water oxidation by macrocyclic nickel(II) complexes: The influence of steric effect on catalytic activity, *Catal. Sci. Technol.*, 2017, **7**, 5585–5593.
20 L. H. Zhang, F. Yu, Y. Shi, F. Li and H. Li, Base-enhanced electrochemical water oxidation by a nickel complex in neutral aqueous solution, *Chem. Commun.*, 2019, **55**, 6122–6125.
21 S. Khan, S. Sengupta, M. A. Khan, M. P. Sk, N. C. Jana and S. Naskar, electrocatalytic water oxidation by mononuclear copper complexes of bis-amide ligands with N4 donor: Experimental and theoretical investigation, *Inorg. Chem.*, 2024, **63**, 1888–1897.
22 K. J. Fisher, K. L. Materna, B. Q. Mercado, R. H. Crabtree and G. W. Brudvig, electrocatalytic water oxidation by a copper(II) complex of an oxidation-resistant ligand, *ACS Catal.*, 2017, **7**, 3384–3387.
23 M. Kondo, H. Tatewaki and S. Masaoka, Design of molecular water oxidation catalysts with earth-abundant metal ions, *Chem. Soc. Rev.*, 2021, **50**, 6790–6831.
24 (*a*) M. Zhang, M.-T. Zhang, C. Hou, Z.-F. Ke and T.-B. Lu, Homogeneous electrocatalytic water oxidation at neutral pH by a robust macrocyclic nickel(II) complex, *Angew. Chem., Int. Ed.*, 2014, **53**, 13042–13048; (*b*) Y. Han, Y. Wu,

W. Lai and R. Cao, Electrocatalytic water oxidation by a water-soluble nickel porphyrin complex at neutral pH with low overpotential, *Inorg. Chem.*, 2015, **54**, 5604–5613; (*c*) D. Wang and C. O. Bruner, Catalytic Water Oxidation by a Bio-inspired Nickel Complex with a Redox-Active Ligand, *Inorg. Chem.*, 2017, **56**, 13638–13641; (*d*) P. Garrido-Barros, S. Grau, S. Drouet, J. Benet-Buchholz, C. Gimbert-Surinach and A. Llobet, Can Ni complexes behave as molecular water oxidation catalysts?, *ACS Catal.*, 2019, **9**, 3936–3945.

25 J. Lin, P. Kang, X. Liang, B. Ma and Y. Ding, Homogeneous electrocatalytic water oxidation catalyzed by a mononuclear nickel Complex, *Electrochim. Acta*, 2017, **258**, 353–359.

26 H. Lee, X. Wu and L. Sun, Homogeneous electrochemical water oxidation at neutral pH by water-soluble NiII complexes bearing redox non-innocent tetraamido macrocyclic ligands, *ChemSusChem*, 2020, **13**, 3277–3282.

27 H.-T. Zhang, Y.-H. Guo, Y. Xiao, H.-Y. Du and M. Zhang, Heterobimetallic NiFe cooperative molecular water oxidation catalyst, *Angew. Chem., Int. Ed.*, 2023, **62**, e202218859.

28 (*a*) S. Adhikari, A. Sarkar and B. B. Dhar, C-H Chlorination using Nickel(II) complexes of tetradentate amido-quinoline ligands, *Chem. Commun.*, 2020, **58**, 4075–4078; (*b*) Monika, A. Sarkar, S. Adhikari and B. B. Dhar, Bio-Inspired Cu(II) amido-quinoline complexes as catalysts for C-H bond hydroxylation, *Dalton Trans.*, 2023, **52**, 540–545.

29 L. Yang, D. R. Powell and R. P. Houser, structural variation in Copper(I) complexes with pyridylmethylamide ligands: Structural analysis with a new four-coordinate geometry Index, τ_4, *Dalton Trans.*, 2007, 955–964.

30 A. J. Bard and L. R. Faulkner, *Electrochemical Methods: Fundamentals and Applications*, Wiley, New York, 2001.

31 (*a*) P. Zanello, *Inorganic electrochemistry. Theory, practice and application*, Royal Society of Chemistry, Cambridge, 2003; (*b*) J. J. Stracke and R. G. Finke, Electrocatalytic water oxidation beginning with the cobalt polyoxometalate $[Co_4(H_2O)_2(P\ W_9O_{34})_2]$10-: identification of heterogeneous CoOx as the dominant catalyst, *J. Am. Chem. Soc.*, 2011, **133**, 14872–14875.

32 J. Hessels, E. Masferrer-Rius, F. Yu, R. J. Detz, J. M. K. Gebbink and J. N. H. Reek, Nickel is a different pickle: Trends in water oxidation catalysis for molecular nickel complexes, *ChemSusChem*, 2020, **13**, 6629–6634.

33 Z. Chen, J. J. Concepcion, H. Luo, J. F. Hull, A. Paul and T. J. Meyer, Nonaqueous catalytic water oxidation, *J. Am. Chem. Soc.*, 2010, **132**, 17670–17673.

34 M. K. Coggins, M. T. Zhang, A. K. Vannucci, C. J. Dares and T. J. Mayer, Electrocatalytic Water Oxidation by a Monomeric Amidate-Ligated Fe(III)-Aqua Complex, *J. Am. Chem. Soc.*, 2014, **136**, 5531–5534.

35 Z. Chen, J. J. Concepcion, X. Hu, W. Yang, P. G. Hoertz and T. J. Meyer, Concerted O atom-proton transfer in the O-O bond forming step in water oxidation, *Proc. Natl. Acad. Sci. U. S. A.*, 2010, **107**, 7225–7229.

36 (*a*) C. Costentin, S. Drouet, M. Robert and J. M. Savéant, Correction to turnover numbers, turnover frequencies, and overpotential in molecular catalysis of electrochemical reactions. Cyclic voltammetry and preparative-scale electrolysis, *J. Am. Chem. Soc.*, 2012, **134**, 19949–19950; (*b*) R. Matheu, S. Neudeck, F. Meyer, X. Sala and A. Llobet, Foot of the wave analysis for mechanistic elucidation and benchmarking applications in molecular water oxidation catalysis, *ChemSusChem*, 2016, **9**, 3361–3369; (*c*) D. Phapale, V. Sharma, A. Saini, S. Sharma, P. Kumar, R. Kumar, M. Shanmugam, A. Draksharapu, A. Dutta, E. J. L. Mclnnes, D. Collison, G. Rajaraman and M. Shanmugam, Capturing the elusive $[RuV{=}O]^+$ intermediate in water oxidation, *ACS Catal.*, 2024, **14**, 11893–11904; (*d*) M. Gil-Sepulcre, P. Garrido-Barros, J. Oldengott, I. Funes-Ardoiz, R. Bofill, X. Sala, P. Benet-Buchholz and A. Llobet, Ligand-Based Electron Transfer in New Molecular Copper-Based Water Oxidation Catalysts, *Angew. Chem., Int. Ed.*, 2021, **60**, 18639–18644.

37 (*a*) H.-Y. Du, S.-C. Chen, X.-J. Su, L. Jiao and M.-T. Zhang, Redox active ligand assisted multi-electron catalysis: A case of CoIII complex as water oxidation catalyst, *J. Am. Chem. Soc.*, 2018, **140**, 1557–1565; (*b*) H. Lee, X. Wu and L. Sun, Homogeneous electrochemical water oxidation at neutral pH by water soluble Ni(II) complex bearing redox non-innocent tetraamido macrocyclic ligands, *ChemSusChem*, 2020, **13**, 3277–3282.

38 M. Ghosh, S. Pattanayak, B. B. Dhar, K. K. Singh, C. Panda and S. Sen Gupta, Selective C–H bond oxidation catalyzed by the Fe-bTAML complex: mechanistic implications, *Inorg. Chem.*, 2017, **56**, 10852–10860.

39 S. Pattanayak, D. B. Chowdhury, B. Garai, K. K. Singh, A. Paul, B. B. Dhar and S. Sen Gupta, Electrochemical formation of FeV (O) and mechanism of its reaction with water during O-O bond formation, *Chem. – Eur. J.*, 2017, **23**, 3414–3424.

40 G. M. Sheldrick, A short history of SHELX, *Acta Crystallogr., Sect. A: Found. Crystallogr.*, 2008, **64**, 112–122.

41 G. Sheldrick, SHELXT - iIntegrated space-group and crystal-structure determination, *Acta Crystallogr., Sect. A: Found. Crystallogr.*, 2015, **71**, 3–8.

42 L. J. Farrugia, ORTEP-3 for windows - a Version of ORTEP-III with a graphical user interface (GUI), *J. Appl. Crystallogr.*, 1997, **30**, 565–568.

43 C. F. Macrae, I. Sovago, S. J. Cottrell, P. T. A. Galek, P. McCabe, E. Pidcock, M. Platings, G. P. Shields, J. S. Stevens, M. Towler and P. A. Wood, Mercury 4.0: from visualization to analysis, design and prediction, *J. Appl. Crystallogr.*, 2020, **53**, 226–235.

44 (*a*) CCDC 2419464: Experimental Crystal Structure Determination, 2025, DOI: **10.5517/ccdc.csd.cc2m6n7r**; (*b*) CCDC 2444267: Experimental Crystal Structure Determination, 2025, DOI: **10.5517/ccdc.csd.cc2n1gbj**.